# Electronic structure, lattice dynamics, and optical properties of a novel van der Waals semiconductor heterostructure: $InGaSe_2$

Wilfredo Ibarra-Hernández,[1,2,*] Hannan Elsayed,[2] Aldo H. Romero,[1,3] Alejandro Bautista-Hernández,[3] Daniel Olguín,[4] and Andrés Cantarero[2]

[1]*Physics Department, West Virginia University, Morgantown, West Virginia 26506-6315, USA*

[2]*Molecular Science Institute, University of Valencia, PO Box 22085, 46071 Valencia, Spain*

[3]*Facultad de Ingeniería, Benemérita Universidad Autónoma de Puebla, Apdo. Postal J-39, Puebla, Pue. 72570, Mexico*

[4]*Departamento de Física, Centro de Investigación y de Estudios Avanzados del Instituto Politécnico Nacional, México DF 07300, Mexico*

(Received 2 February 2017; revised manuscript received 18 April 2017; published 14 July 2017)

There is a growing interest in the property dependence of transition metal dichalcogenides as a function of the number of layers and formation of heterostructures. Depending on the stacking, doping, edge effects, and interlayer distance, the properties can be modified, which opens the door to novel applications that require a detailed understanding of the atomic mechanisms responsible for those changes. In this work, we analyze the electronic properties and lattice dynamics of a heterostructure constructed by simultaneously stacking InSe layers and GaSe layers bounded by van der Waals forces. We have assumed the same space group of GaSe, $P\bar{6}m2$ as it becomes the lower energy configuration for other considered stackings. The structural, vibrational, and optical properties of this layered compound have been calculated using density functional theory. The structure is shown to be energetically, thermally, and elastically stable, which indicates its possible chemical synthesis. A correlation of the theoretical physical properties with respect to its parent compounds is extensively discussed. One of the most interesting properties is the low thermal conductivity, which indicates its potential use in thermolectric applications. Additionally, we discuss the possibility of using electronic gap engineering methods, which can help us to tune the optical emission in a variable range close to that used in the field of biological systems (NIR). Finally, the importance of considering properly van der Waals dispersion in layered materials has been emphasized as included in the exchange correlation functional. As for the presence of atoms with important spin-orbit coupling, relativistic corrections have been included.

DOI: 10.1103/PhysRevB.96.035201

## I. INTRODUCTION

Since the discovery of graphene, there has been an intense activity within the scientific community in the field of low-dimensional materials, specially on metal dichalcogenides [1]. New interesting properties have been discovered, so far, such as the existence of topological insulators [2], band gap engineering [3], van der Waals interlayer frictional forces [4], etc. In most of these studies, the role played by a few monolayers, or even one monolayer, has attracted the interest of physicists and chemists due to the changes in the optical properties as the dimensionality is reduced [5,6]. New unexpected properties arise with interest from both the fundamental point of view and the envisioned of new applications [1]. Among the most promising materials examined nowadays, $MoTe_2$ [7], $WS_2$ and $MoS_2$ [8–11], $ZrS_2$ and $ZrSe_2$ [12], $Bi_2Te_3$ [13–15], $Bi_2Se_3$ [16], PbSe [17,18], GaSe [19–22], InSe [23–26], GaS [27], GeS [28], and other layered compounds have been extensively studied, where particular attention has been paid to the properties of one or a few material layers. On the other hand, in connection to graphene and in particular the possibility to stick graphene to boron nitride or other single-layer materials, a renewed interest on van der Waals heterostructures has arisen. In a recent work, several researchers have demonstrated the fractal character in the stacking of graphene on BN and the appearance of Hofstadter butterflies [29,30], which were predicted in the past but never grown or measured [31]. X. Li *et al.* have recently grown a few layers of GaSe [20,21] and stack the layers forming different orientation angles between layers, which can allow the formation of large in plane supercells, giving rise to new interesting phenomena.

Concerning the applications of some of the mentioned layered compounds, topological insulators are believed to play in the future an important role in spintronics, in particular, $Bi_2Te_3$ [32]. Bismuth telluride is, on the other hand, a very well known thermoelectric material, with a renewed interest nowadays [33–35]. Since $InGaSe_2$ has a more complex structure compared to InSe or GaSe (and thus a lower sound velocity for the acoustic phonons), we can also expect that $InGaSe_2$ would be a good thermoelectric material. We discuss more about this possibility in the lattice dynamics sections. Additionally, the electronic gap seems to be in the region of interest for the fabrication of lasers for biological systems and telecommunications (NIR).

In this work, we propose a new van der Waals heterostructure composed by stacking GaSe layers and InSe layers, keeping the space group of GaSe ($P\bar{6}m2$). We believe that this type of heterostructure can be grown by van der Waals epitaxy [36], as it has recently been demonstrated to work in the case of $Bi_2Se_3$ [37], or following the method given in Refs. [20,21]. The growth of InSe/GaSe quantum wells has been proposed in the past [38] and even a linear chain model for the proposed structure of the wells has been calculated [39]. The growth of InSe on GaSe and GaSe on InSe [40] has been demonstrated experimentally, and there is also a theoretical paper of an InSe/GaSe superlattice within the framework of the effective mass approximation [41]. In this work, we present the calculation of the electronic band structure and the lattice

*Corresponding author: wilfredo.ibarrahernandez@mail.wvu.edu

 

dynamics of an $InGaSe_2$ crystal by means of density functional theory. The elastic constants, thermal conductivity, and optical properties have also been calculated.

## II. THEORETICAL DETAILS

In the calculations reported in this work, we have used two different but complementary *ab initio* codes. The main reason is that, in one of then, we can provide a very reasonable value for the gap with low computational cost using the modified Becke-Johnson (mBJ) correction (WIEN2K-mBJ) [42], while in the other we can introduce van der Waals corrections, needed to provide accurate interlayer distances, which are essential to properly calculate the lattice dynamics and elastic properties.

The total energy and vibrational *ab initio* calculations reported here have been performed within the framework of density functional theory (DFT) and the projector-augmented wave (PAW) [43,44] method as implemented in the Vienna *ab initio* simulation package (VASP) [45–48]. We used a plane-wave energy cutoff of 650 eV to ensure very high convergence in forces and energies in all our calculations. The exchange and correlation energy was described within LDA (VASP-LDA) [49] and with GGA with the Perdew-Burke-Ernzerhof (PBE) functional (VASP-PBE) [50]. We have used an In pseudopotential with $5s^2 5p^1$ valence, while for Ga and Se, the valence states of the pseudopotentials are $3d^{10}4s^2 4p^1$ and Se $4s^2 4p^4$, respectively. Due to the presence of van der Waals interactions, we have also considered a nonlocal correlation functional as introduced by Dion *et al.* [51] and with the specific form for the exchange functional as proposed and implemented in VASP by Klimeš *et al.* (VASP-vdW) [51–53]. The Monkhorst-Pack scheme was employed for the Brillouin-zone (BZ) integrations [54] with a $12\times12\times3$ mesh centered at the $\Gamma$ point (in the calculation of the elastic constants a $14\times14\times4$ mesh has been used). In the relaxed equilibrium configuration, the forces were less than 1 meV $Å^{-1}$ per atom in each of the Cartesian directions and each component of the stress tensor was relaxed to values smaller than 2 bars. Highly converged results on forces were required for the calculations of the dynamical matrix using the direct force constant approach (or supercell method) as implemented in the PHONOPY code [55,56] interfacing with VASP. For the bulk case, we have considered a $3\times3\times2$ supercell, and for the anharmonic properties we did use a $2\times2\times2$ supercell, and we took into account interactions up to the fourth neighbor. For the anharmonic part and, therefore, the calculation of the thermal conductivity, we use the PHONO3PY code that solves the Boltzmann transport equation for phonons iteratively through the second- and third-order interatomic force constants. Then, the group velocities and phonon lifetime, and ultimately the thermal conductivity, can be obtained [56]. The optimized geometries obtained from this code were then used for further analysis.

On the other hand, we have made use of a full potential linearized augmented plane-wave method (FP-LAPW) also for DFT as implemented in the WIEN2K code [57]. In this method, the wave functions, charge density, and crystal potential are expanded in spherical harmonics within nonoverlapping muffin-tin spheres and in plane waves in the interstitial regions between the spheres. In this code, core and valence states can be managed in a different way. Core states are treated fully relativistic, while valence states are treated in a scalar relativistic approach as it is discussed in Refs. [58,59], as well as for the VASP code. The exchange-correlation energy has been calculated using the local density approximation (WIEN2K-LDA) [49] and the generalized gradient approximation (WIEN2K-PBE) correction of Perdew *et al.* [50]. The convergence of the total energy in terms of the variational cutoff-energy parameter has been guaranteed by using an appropriate set of $k$ points in the calculations. The In $4p$ states and the Ga $3d$ states were treated as valence-band states using the local orbital extension of the LAPW method [57], and spin-orbit (relativistic) corrections have been taken into account. The plane-wave cutoff used was 9 Ry. A set of 70 $k$ points was used to calculate the total energy for $InGaSe_2$, this $k$ points set is equivalent to a $13\times13\times2$ Monkhorst-Pack [54] grid.

## III. CRYSTAL STRUCTURE

Figure 1 shows four unit cells of the proposed $InGaSe_2$ structure in the $xy$ plane and one extra GaSe layer in the

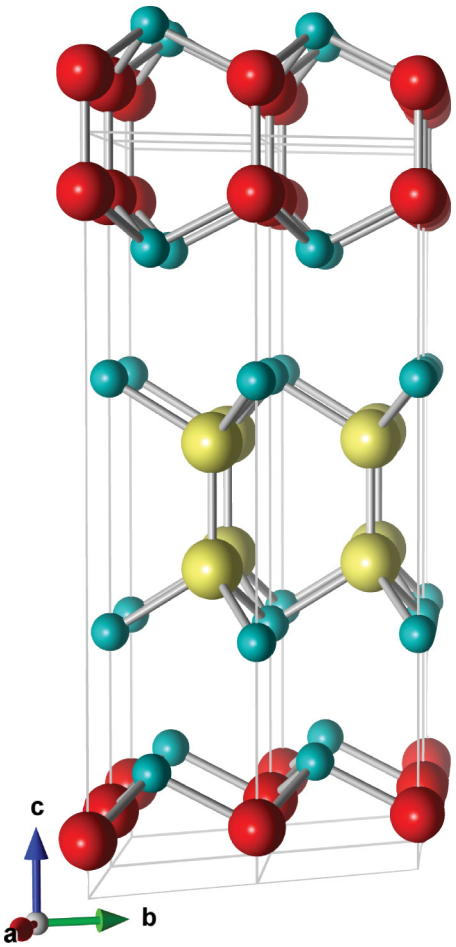


FIG. 1. $InGaSe_2$ supercell with space group No. 187 ($P\bar{6}m2$) showing the stacking of GaSe/InSe. We can observe the interlayer separation of the Se-Se atoms due to van der Waals forces. Indium, gallium, and selenium atoms are represented by yellow, red, and turquoise balls, respectively.

$z$ direction, in order to depict the layered structure. The shown unit cells in the plane allow us to observe the interatomic bonds. The layer stacking (if all layers were of GaSe) corresponds to the $\varepsilon$-polytype. The layers consist of a hexagonal lattice of Se, where three Se are bound to an In atom, an In-In (Ga-Ga) bond perpendicular to the layer structure, and further bonds to the upper hexagonal layer of Se in a symmetric pattern. In a layer, we have the same stacking, independent of whether we have InSe or GaSe, although the bond distances are different. The two layers of Se are bound through van der Waals forces and thus, the Se-Se interlayer distances are larger than the other bond distances (Se-Se in plane more precisely). The space group is $P\bar{6}m2$. The proposed crystal structure differs from the superlattice proposed by Gashimzade *et al.* [41], where the stackings of InSe and GaSe are in their bulklike crystal structure ($\gamma$-InSe/$\varepsilon$-GaSe). We choose this particular configuration since the symmetries of individual monolayers of InSe and GaSe are similar ($D_{3h}$ point group) and such similarity breaks in the bulk compounds [60].

The In atom has a larger atomic radius than Ga, thus, the unit cell of GaSe is smaller than that of InSe. Once the structure of $InGaSe_2$ has been optimized, it is expected that the layers of GaSe will be tensioned in the plane and thus there will be a compression in the $z$ direction, while in the case of an InSe layer, there will be a compression in the plane and a tension in the $z$ direction. This can be concluded from the energy difference of the $InGaSe_2$ heterostructure with respect to the pristine InSe and GaSe compounds, which is higher in energy by 0.1 eV per formula unit. As a first approximation, the volume of the unit cell must be conserved (within the elastic limit) and only the stretching of the different layers will be responsible for the changes in the crystal cell, but as we will show below, even after this structural rearrangement, the system is thermally and elastically stable. These changes in the parameters are not unusual in low dimensional systems as it happens to other cases as in $PbSe/WSe_2$ [61], $PbSe/NbSe_2$ [62], graphene/BN [63], etc. In this work, we have also calculated the electronic structure of $\varepsilon$-InSe for completeness (see Supplementary Material, where the electronic structures of $\varepsilon$-InSe and $\varepsilon$-GaSe are compared).

## IV. STRUCTURE OPTIMIZATION

We perform a full structural optimization of the lattice parameters and internal coordinates of $InGaSe_2$ within the VASP code as this code includes the van der Waals functionals (VASP-vdW), an important element in layered materials. With the aim to assure consistency between the two used codes, we have performed structural relaxation for InSe and GaSe in the $\epsilon$ crystal phase using PBE and LDA as the exchange-correlation functionals and without considering Van der Waals corrections. The results were compared to available experimental data. We have found that with VASP-LDA (WIEN2K-LDA), GaSe shows lattice parameters equal to $a = 3.72$ Å (3.65 Å) and $c = 15.63$ Å (15.21 Å), while VASP-PBE (WIEN2K-PBE) gives $a = 3.82$ Å (3.81 Å) and $c = 17.94$ Å (16.20 Å). Experimental measurements of the structural parameters give $a = 3.74$ Å and $c = 15.919$ Å. For the case of InSe, we have obtained the lattice constant values equal to $a = 3.99$ Å (3.98 Å) and $c = 16.26$ Å (17.24 Å) for VASP-LDA (WIEN2K-LDA) and $a = 4.10$ Å (4.16 Å) and $c = 18.63$ Å (17.36 Å) for VASP-PBE (WIEN2K-PBE), while the experimentally reported values are $a = 4.04$ Å and $c = 16.90$ Å. These results show that the structures obtained with standard PBE and LDA are similar between the two codes. The main differences are in the estimation of the $c$ parameter. Nevertheless, it has been observed that the inclusion of vdW corrections improves the $c$ parameter for various arrangements of InSe and GaSe [64]. In that respect, we have also included in our analysis vdW corrections for $InGaSe_2$. In general, we have found that VASP-LDA systematically underestimates the lattice parameters with respect to experimental measurements [65,66].

TABLE I. Nearest-neighbor and next-nearest-neighbor distances for $InGaSe_2$ and its parent compounds calculated with WIEN2K-PBE (W) and the VASP-vdW (V), respectively. All values are given in angstroms. The label $Se\text{-}Se_l$ refers to the intralayer distance (within the $xy$ plane), $Se\text{-}Se_i$ refers to the shorter "bond" distance between two Se atoms in different layers, while interlayer refers to the distance, in the $c$ direction, between two adjacent Se-Se layers.

| Crystal | Ga-Ga | Ga-Se | In-In | In-Se | $Se\text{-}Se_l$ | $Se\text{-}Se_i$ | Interlayer |
|---|---|---|---|---|---|---|---|
| $\varepsilon$-GaSe (W) | 2.431 | 2.515 | | | 3.810 | 3.918 | 3.240 |
| $\varepsilon$-GaSe (V) | 2.480 | 2.511 | | | 3.841 | 4.023 | 3.357 |
| $\varepsilon$-InSe (W) | | | 2.605 | 2.732 | 4.160 | 4.222 | 3.473 |
| $\varepsilon$-InSe (V) | | | 2.825 | 2.701 | 4.111 | 3.953 | 3.161 |
| $InGaSe_2$ (W) | 2.488 | 2.551 | 2.799 | 2.667 | 3.945 | 3.868 | 3.126 |
| $InGaSe_2$ (V) | 2.488 | 2.552 | 2.818 | 2.669 | 3.970 | 4.020 | 3.303 |

The work of Srour *et al.* shows that the inclusion of vdW corrections (within the Grimme's approximation) improves the accuracy of the interlayer stacking distance with respect to the results obtained with the PBEsol functional for GaSe [64]. The use of mBJ approximation corrects the systematic underestimation of the electronic band gap showed in DFT calculations, which improves the agreement with experimental data at a lower computational effort than the hybrid exchange correlation functionals [67].

In Table I, we summarize the interatomic distance results for $\varepsilon$-GaSe, $\varepsilon$-InSe, and $InGaSe_2$ obtained from VASP-vdW (with a LDA pseudopotential) and WIEN2K-PBE. Here, we would like to remark that, even though vdW functionals in the VASP code are built on top of GGA functionals, according to VASP documentation, either PBE or LDA pseudopotentials can be used since only the sum of the pseudovalence density and partial core density are used for the evaluation of the vdW energy term [68]. The $InGaSe_2$ unit cell parameters obtained using the WIEN2K-PBE are $a = 3.9945$ Å ($Se\text{-}Se_l$ distance) and $c = 16.61$ Å, while those calculated using VASP-vdW are $a = 3.97$ Å and $c = 16.89$ Å. We found that for our system, within the VASP code (VASP-LDA compared with VASP-vdW), the inclusion of vdW corrections systematically increases the lattice parameters. We have observed the same trend for InSe, GaSe, and $InGaSe_2$. We observe an increase of 3.3% and a more abrupt increase of 4.75% in the $a$ and $c$ parameter, respectively, for $InGaSe_2$. The work of Srour *et al.* [64] shows that the values obtained with VASP-vdW, for different structures of GaSe and InSe, are in better agreement

with experimental measurements than those obtained with WIEN2K-PBEsol, especially the interlayer distances. We would like to remark that Sour *et al.* have used the vdW Grimme's correction on top of the PBE functional, while here, we have used the nonempirical vdW nonlocal correlation functional as proposed by Dion *et al.* [51–53], where the long-range part is taken from the single-pole approximation to DFT. However, we have observed similar trends between the two methods. For example, we have noticed that for GaSe, the use of vdW functional (VASP-vdW) reduces the interlayer distance, which is the same behavior observed by Srour *et al.* The authors report the same behavior for the different configurations of InSe, which leads (at least in the case with experimental data) to a worse agreement with experimental measures for the same interlayer distance with respect to PBEsol results. In our case, the use of the Van der Waals functional increases the interlater distance for InSe with respect to the Grimme's approximation, suggesting a possible better agreement to experimental data. For $InGaSe_2$, the interlayer distance is the largest one (not the same that Se-Se "bond" distance), the value obtained with VASP-vdW is 3.303 Å, while that calculated with WIEN2K-PBE is 3.126 Å. Though the van der Waals forces should not affect much the electronic properties, we have used the optimized crystal structures obtained from VASP-vdW as the used geometry on any further analysis. This can also be straightened out by comparing the electron charge distribution obtained from the VASP code for the cases with and without vdW corrections. No noticeable difference were observed (see Ref. [69]).

## V. ELECTRONIC STRUCTURE

This section is devoted to the electronic structure, where the band structure was obtained from VASP-vdW, while the optical spectra were obtained from WIEN2K-mBJ, although with the optimized parameters given by the VASP code, since the difference in the interlayer distance changes notably. The parameters obtain with the VASP code are more reliable in the case of van der Waals semiconductors.

### A. Atomic contributions to the bands

The atomic contribution to the bands calculated with VASP-vdW is shown in Fig. 2. The atomic contribution has been quantified using the size of the symbol in the figure. We found that the Ga contribution to the electronic bands is small around the Fermi level (zero energy in Fig. 2) compared with the contribution of In or Se. We also observe that the main contribution to the valence and conduction bands comes from selenium atoms. This contribution has *p* character, as it can be seen in Ref. [69].

### B. Electronic band structure

In Ref. [69], we compare the electronic band structure of $InGaSe_2$ with that of $\varepsilon$-InSe and $\varepsilon$-GaSe. Here, we limit the representation of the band structure to the $InGaSe_2$, which is the purpose of the present work. While the band structures obtained from both codes are very similar, here we only use the WIEN2K (WIEN2K-PBE and WIEN2K-mBJ) because it gives the necessary information to understand the optical response.

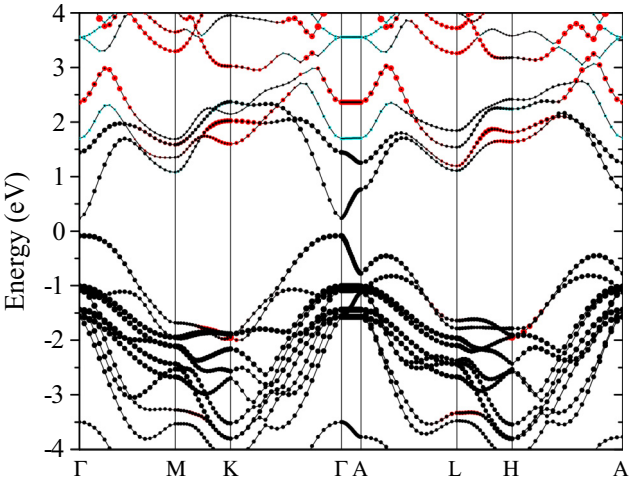


FIG. 2. Electronic band structure obtained with VASP-vdW for $InGaSe_2$. The indium contribution to the bands is represented by red circles, the selenium contribution is in black, and the Ga contribution is in blue.

In Fig. 3, we show the electronic band structure of $InGaSe_2$, with (black-solid lines) and without (red-dashed lines) the mBJ [42] correction as obtained from the WIEN2K code (WIEN2K-mBJ and WIEN2K-PBE, respectively). The value for the direct band gap of $InGaSe_2$ ($\approx$1.2 eV) is in an interesting range for biological applications and telecommunications. Modifying the system to different InSe/GaSe stacking, we should be able to modify the gap up to 40% (going from the InSe to the GaSe electron band gap). In both cases we show a direct band gap located at the Γ point of the BZ with a small effective mass for the electrons.

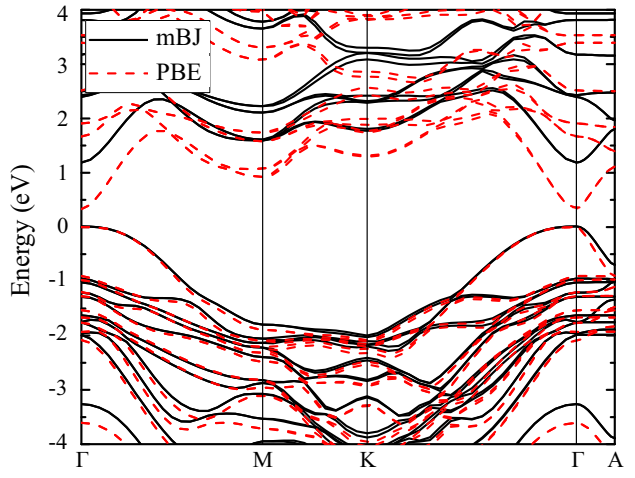


FIG. 3. Electronic band structure of $InGaSe_2$, taking into account the mBJ exchange correlation potential (WIEN2K-mBJ, solid-black line). The value of the gap, $E_g = 1.207$ eV, is compared with that obtained without the mBJ correction (0.369 eV). Dashed-red lines correspond to the bands obtained before applying the mBJ correction (WIEN2K-PBE).

TABLE II. Comparison of the band gaps calculated for GaSe, InSe, and $InGaSe_2$. The value of the InSe gap has been assumed to be the same as that of the $\gamma$-polytype [70]. All values are in eV.

| Structure | $E_g^{\text{exp}}$ | $E_g^{\text{PBE}}$ | $E_g^{\text{PBE-mBJ}}$ | $E_g^{GW}$ |
|---|---|---|---|---|
| $\varepsilon$-GaSe | 2.12 | 0.785 | 1.463 | 2.34 |
| $\varepsilon$-InSe | 1.20 | 0.247 | 1.019 | |
| $InGaSe_2$ | | 0.369 | 1.207 | |

In Table II, we compare the calculated band gaps of InSe, GaSe, and $InGaSe_2$ and show some experimental data and previous calculations, when available.

Applying the mBJ correction to the layered compounds gives an improved value for the electron band gap, but in the case of GaSe is still far from the experimental value [71]. On the other hand, the value calculated with the $GW$ correction [72] is a 10% higher than the experimental gap of GaSe. The band gap of $\gamma$-InSe is close to 1.2 eV [70], but there are no experimental data in the case of $\varepsilon$-InSe. Since the packing of the structures is very similar, we assume that the gaps are also similar (as we have discussed before, the vdW corrections should not modify much the electronic structure). If we apply the same correcting factor to obtain the experimental gap of GaSe, the band gap of $InGaSe_2$ would be of the order of 710 nm/1.75 eV, in between the GaSe and InSe gaps. This value is in the range of emission of lasers used in biology and telecommunications. In any case, it is clear that the mBJ correction needs to be reparametrized for the case of layered compounds following the work of Tran and Blaha [42]. It is well known that standard DFT tends to underestimate the electronic band gap. We found that the band gap obtained with VASP-vdW is very similar to the one obtained with WIEN2K-PBE (0.383 eV). This is expected since both calculations were done with PBE pseudopotentials and the only correction is on the crystal structure (only in VASP-vdW).

### C. Optics

In this section, we have calculated the real and imaginary parts of the dielectric function of $InGaSe_2$ as obtained from the WIEN2K code (WIEN2K-mBJ). The optical properties are given in terms of the complex dielectric function $\varepsilon(\omega) = \Re\varepsilon(\omega) + \Im\varepsilon_2(\omega)$, which in the case of a uniaxial crystal is a tensor with $\varepsilon_{xx} = \varepsilon_{yy} \neq \varepsilon_{zz}$.

To calculate the imaginary part of the dielectric function we have to integrate over all possible transitions. The intraband transitions are only important for metals, in the case of semiconductors we have to consider only transitions from the valence to the conduction band. Thus the imaginary part of the dielectric function is given by the expression

$$\Im\varepsilon_{zz}(\omega) = \frac{4\pi e^2}{m^2\omega^2} \sum_{c,v} \int_{\text{BZ}} d^3\boldsymbol{k} |\langle v_k | P_z | c_k \rangle|^2 \delta\left(E_{c_k} - E_{v_k} - \hbar\omega\right), \tag{1}$$

where $e$ and $m$ are the electron charge and mass, respectively, and $\hbar\omega$ is the energy of the incoming photon. $\langle v_k | P_z | c_k \rangle$ is the interband dipole allowed transition, as in the present case. The expression for $\Im\varepsilon_{xx}(\omega)$ is equivalent by substituting $P_z$ by $P_x$.

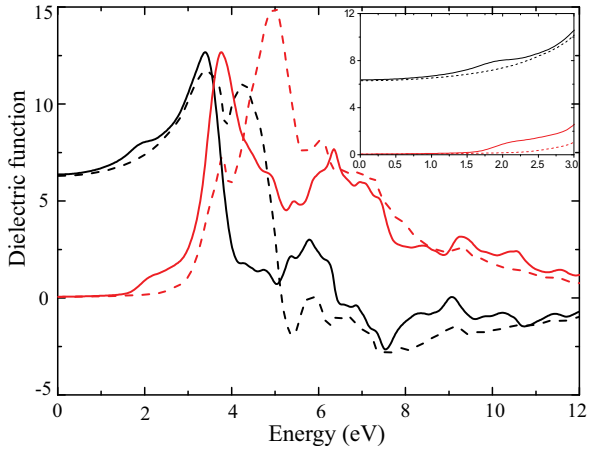


FIG. 4. Real and imaginary parts of $\varepsilon(\hbar\omega)$, in units of the dielectric permittivity of vacuum, corresponding to $InGaSe_2$. The real parts $\Re\varepsilon_{zz}(\hbar\omega)$ and $\Re\varepsilon_{xx}(\hbar\omega)$ are shown in black-solid and black-dashed lines, respectively. The imaginary parts $\Im\varepsilon_{zz}(\hbar\omega)$ and $\Im\varepsilon_{xx}(\hbar\omega)$ have been plotted in red-solid and red-dashed lines, respectively.

The real part can be written in terms of the imaginary part through the Kramers-Kronig relation,

$$\Re\varepsilon(\omega) = 1 + \frac{2}{\pi}\mathcal{P}\int \frac{\omega'\Im\varepsilon(\omega')}{\omega'^2 - \omega^2} d\omega', \tag{2}$$

where $P$ in front of the integral means its principal value. In Fig. 4, we show $\Re\varepsilon$ and $\Im\varepsilon$ for polarizations in the $z$ and $x$ directions. The origin of energies was taken at the top of the valence band. The red solid line represents $\Im\varepsilon_{zz}(\omega)$ while the red dash line is $\Im\varepsilon_{xx}(\omega)$.

On resolving the optical spectra shown in Fig. 4, it is clear that the onset of the edge band occurs around 1.2 eV and the region of sun optical absorption matches the optical region with respect to this material, indicating that $InGaSe_2$ in this configuration should absorb in the visible region. Around the gap, close to 1.2 eV, $\Im\varepsilon_{zz}$ starts to grow and there is a maximum in the region close to 3.7 eV, which corresponds to the interband transition from the $p$ states of Se and the $s$ states of Ga (see the DOS in Ref. [69]). After this maximum, the dielectric function decreases again. At 12 eV, we have basically the electronic contribution ($\varepsilon_\infty$). In the case of $\Im\varepsilon_{xx}(\omega)$, the value of the dielectric function is shifted at higher energies since the transition is dominated by the split-off valence band, as in the case of III-V compounds [73]. The top of the valence band has $p_z$ character, while the split-off band has $p_x + p_y$ character (Fig. 3 in Ref. [69]). Figure 4 also shows the real part $\Re\varepsilon$, which can be obtained from the imaginary part from Eq. (2) and represents the changes in the refractive index of the material. We have also found the real part of the dielectric function becomes negative at energies of 5.11 and 6.5 eV for out of plane and in plane, respectively. The negative dielectric function has been also observed theoretically for $\varepsilon$-GaSe at an energy of 7 eV [74]. Experimentally, it has been measured that the real part of the dielectric function becomes negative in $\varepsilon$-GaSe [75]. As far as we know, there is no ellipsometry information of the dielectric function for $\varepsilon$-InSe and even for $\beta$-InSe the available data are rare.

## VI. LATTICE DYNAMICS

Starting from crystal symmetry considerations and by using group theory [76], we obtain the following symmetry characters for the Γ point:

$$\Gamma = 4A_1' + 4A_2'' + 4E' + 4E'', \tag{3}$$

since the space group is the $P\bar{6}m2$ (with Wyckoff positions 2i, 2g, and 2h). We have eight atoms inside the unit cell and thus 24 vibrational modes. The $A$ modes are one dimensional (they vibrate in the $c$ direction, perpendicular to the layers) while the $E$ modes are two dimensional (they vibrate in the $ab$ plane). The acoustic modes are $A'' + E'$, thus the remaining modes (21) are Raman (R) or/and infrared (IR) active. Actually, since there is no center of inversion, some of the modes can be both IR and R active. The $4A_1' + 4E''$ (12) modes are only Raman active (there is a change of polarizability but they do not carry a dipole moment), the $3A_2''$ (3) modes are IR active (they carry a dipole moment but there is no change of polarizability), and the $3E'$ (6) modes are both R and IR active (they carry a dipole moment and the vibrations modify the Raman polarizability). This is basically concluded from group theory, but we know that polar modes can split into TO and LO. These are the $3A'' + 3E'$ modes. In backscattering configuration in Raman [77], in the case of an $A''$ mode, if the laser light has the $c$ direction, we observe an $A''(LO)$ mode (in the present material), while in the case the light travels in the $a$ or $b$ plane we will observe the $A''$(TO). The same happens in the case of an $E'$ mode. If the vibration is along $a$ and the light comes along the $a$ axis, we have an $E'$(LO) mode, while in the case the light beam travels along the $b$ or $c$ axis, we will observe the $E'$(TO). In the case of GaSe, the LO-TO splitting was observed in an $E'$ mode [78] [they called them $E'^{(4)}$(LO) and $E'^{(4)}$(TO), in the case of InSe, as far as we know, there are no Raman data for the $\varepsilon$-polytype. In any case, the behavior of the phonons in this heterostructure resembles those from the pristine compounds. Therefore it is expected that the phonon polarization can be also correlated to exciton dephasing [79].

### A. Phonon dispersion relations

Figure 5 shows the phonon dispersion relations of $InGaSe_2$ calculated from the PHONOPY code (interfaced with VASP-vdW) [55], including the LO-TO splitting obtained by considering the Born effective charges. There are 24 modes, as it can be observed in any of the directions outside the Γ point, where there are several degenerate modes. First of all, there is not a single imaginary mode, which indicates the thermal stability of this compound. There is a mode at the $A$ point, which is softer compared with other acoustic modes. Some of the optical modes have also an important drop in the phonon eigenvalue, in particular at the Γ symmetry point. Figure 5 also shows a phonon band gap from ≈5 to ≈5.5 THz. A similar phonon dispersion was reported for SnSe [80,81], a compound that has been found to have a remarkable low thermal conductivity and that, recently, has been proposed as a good thermoelectric material at temperatures around 700 K [82]. In this case, it has been established that more than the phonon band gap, the interaction between optical and acoustic phonon modes is mainly responsible for the drastic decrease of the thermal

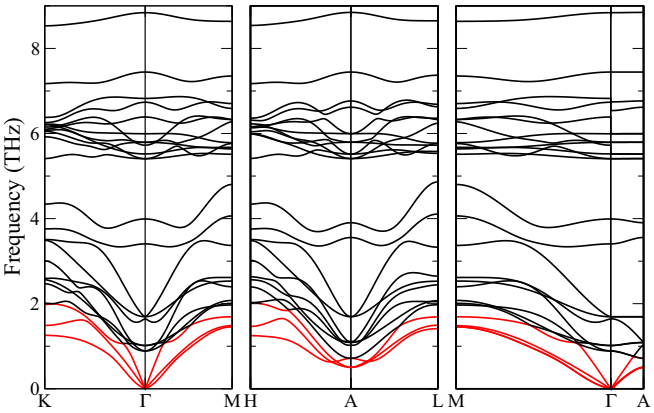


FIG. 5. Phonon dispersion relations of $InGaSe_2$ as obtained from the PHONOPY code as interfaced with VASP (see Ref. [69]). The three acoustic branches are in red for its easy identification.

conductivity [83]. This feature is shared by the compound that we propose and the mentioned SnSe. The $c$ axis is very long compared to $a$ and $b$, therefore the reciprocal direction Γ-$A$ is small compared to any other direction in the plane (for instance the Γ-$M$). Nevertheless, we can clearly observe at the right side of Fig. 5 the splitting of the two highest $E'$ modes. The low frequency $E'$ mode has a very small splitting and it cannot be observed in the dispersion relations. When coming from the $A$-Γ direction, the $E'$ modes are degenerate, but when the modes come from the $M$-Γ direction, we can see the LO-TO splitting. There is also a splitting in one of the IR $A''$ modes. Our calculations suggest that the material could be experimentally synthesized since we found only positive frequencies in the entire Brillouin zone, which is an indication of dynamic stability. The nonlinear behavior of the lowest energy acoustic phonon modes near Γ is not exclusive to our system. It has also been observed in other layered materials, such as in different stacking configurations for graphene [84] or $KC_8$ and $Rb_8$ [85], or the BiSb layered structure [86], and it is related to the weak forces between the layers and the rigid layer (in-plane layer) that moves as a rigid unit [87,88]. Nevertheless, the nonlinear behavior that we observe is not as abrupt as in the previously mentioned examples, since we have bilayers stacking along the $c$ axis. In particular, the nonlinear acoustic phonon modes are also reported in layered $\varepsilon$-GaSe calculated by first principles [89]. We must remark that the mentioned calculations show very good agreement with experimental measurements obtained from neutron scattering [90].

### B. Phonon modes in $InGaSe_2$

In this section, the different optical phonons at the Γ point will be analyzed and visualized. The frequencies of the optical modes are listed, in THz (1 THz = 33.35641 $cm^{-1}$), in Table III.

The frequency depends on the distortion of the lattice during the atomic movement. Then, as a general rule, $A$ modes involving the same atomic movements have a larger frequency than $E$ modes (it is like stretching versus bending/sliding). The LO-TO splitting has not been included in the

TABLE III. Calculated modes of $InGaSe_2$, ordered by increasing frequency, using the program PHONOPY [55]. There are Raman active (R) modes, infrared active (IR), and some are both R and IR active because the space group has no center of inversion, they are not mutually excluded. Charge effective masses have not been taken into account (see Ref. [69]). Activity "A" means acoustic.

| Mode | Frequency (THz) | Activity |
|---|---|---|
| $E'$ | 0 | A |
| $A_2''$ | 0 | A |
| $E'$ | 0.897 | IR, R |
| $E''$ | 1.017 | R |
| $A_2''$ | 1.644 | IR |
| $E''$ | 1.693 | R |
| $A_1'$ | 3.406 | R |
| $A_1'$ | 3.991 | R |
| $E''$ | 5.408 | R |
| $E'$ | 5.520 | IR, R |
| $E''$ | 5.793 | R |
| $E'$ | 5.995 | IR, R |
| $A_2''$ | 6.388 | IR |
| $A_2''$ | 6.735 | IR |
| $A_1'$ | 7.445 | R |
| $A_1'$ | 8.840 | R |

table, for simplicity, since the movement of the mode will be the same, only the propagation direction and frequencies will change (see Figs. 5 and 6). Starting from the highest frequency, there are two $A_1'$ modes, one at 8.44 THz and the other at 7.44, which are Raman active (see Table III). The mode with the highest frequency (8.44 THz) corresponds to the vibration of the GaSe layer, while the mode at 7.44 THz corresponds to the vibration of the InSe layer (see Fig. 6). These two modes are nonpolar since the dipole moment from above and under the mirror plane between the In-In interlayer compensates each other. The reason why the GaSe layer vibrates at a higher frequency is the lower mass of Ga compared to the mass of In. At lower frequencies, we have two $A_2''$ modes. In both modes, the cations vibrate against the anions, but in the mode at 6.73 THz, the dipole moments created by the two layers are compensated, while in the 6.40 THz mode the two dipole moments add up and for this reason the mode splits into TO and LO (Ref. [69]). Lowering the frequency, we have two more Raman active ($A_1'$) modes, at 3.99 and 3.40 THz, and the last optical $A_2''$ mode, at 1.64 THz. There is one $A_2''$ acoustic mode. From group theory, the IR and Raman modes are easily distinguished because under the mirror plane operation, the Raman mode is symmetric while the IR is antisymmetric.

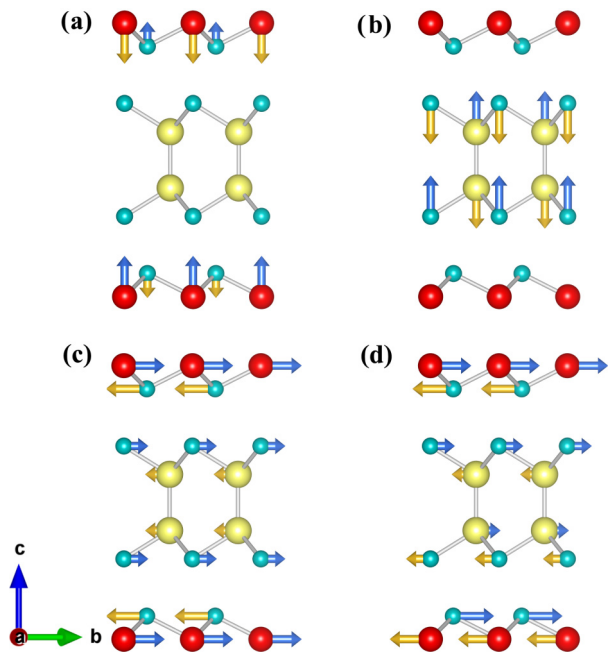


FIG. 6. $A_1'$ and $E'$ eigendisplacements at Γ. (a) $A_1'$ mode with a frequency of 8.84 THz. This mode corresponds to the vibration of GaSe layers. (b) $A_1'$ mode with frequency of 7.74 THz, which corresponds to the vibration of InSe layers. (c) $E'$ (5.99 THz) and (d) $E''$ (5.79 THz) modes. In the $E'$ mode, the two dipole moments (from above and below the mirror plane) adds, while in the $E''$ the dipoles subtract since anion and cation moves in opposite direction. (The color of the atoms are the same than in Fig. 1).

The $3E'$ modes appear at 5.99, 5.52, and 0.89 THz with the corresponding LO/TO splitting. In Fig. 6(c), we show the highest frequency $E'$ mode. From the atomic movement, we can see that the two dipole moments add, and at the same time there is a change in the Raman polarizability, therefore, this mode exhibits Raman and IR response. We have also drawn in Fig. 6(d) the highest frequency $E''$ nonpolar mode (at 5.79 THz). Although there is a dipole moment, they compensate and thus, it is only Raman active. The other $E''$ modes appear at 5.40, 1.69, and 1.01 THz.

In Figs. 6(a) and 6(b), we show the atomic movement corresponding to the two $A_1'$ phonon of higher frequency. In these modes, all cations move in the opposite direction of the anions, but the two dipole moments cancel out; however, the Raman polarizability is nonzero, it is thus a Raman allowed mode. As explained above, the high frequency mode corresponds to vibration of the GaSe, while that at lower frequency corresponds to the atomic movement of the InSe layer (the mass of In is larger than that of Ga).

### C. Thermal conductivity

It was common to neglect optical phonons for the calculation of the thermal conductivity due to their low group velocities, phonon occupation and its large excitation energy [91,92]. However, in cases where optical phonons have frequencies comparable with acoustic ones, they necessarily must be taken into account. We showed in a previous publication that, optical phonons provide important scattering channels for acoustic modes, which significantly reduces the thermal conductivity in $LiMg_2$ [83]. We have calculated the phonon contribution to the thermal conductivity $\kappa$, as implemented in the PHONO3PY code [56]. In Fig. 7, we show $\kappa$ as a function of temperature from 50 to 800 K. At low temperatures, they are of the order of a typical semiconductor, but if we pay attention at the high-temperature region, starting at 300 K, we can observe that the value of $\kappa$ is of the order, or even lower, than that of a polymer [93]. This is a remarkable result, since the lattice contribution to the thermal conductivity is extremely low. Figure 7 shows that the out-of-plane $\kappa$ exhibits

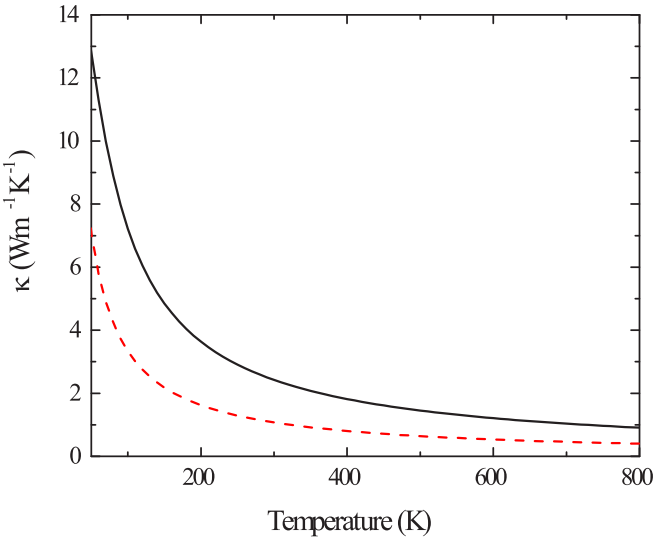


FIG. 7. Thermal conductivity of $InGaSe_2$. Black solid line and red dashed line correspond to values along the $a$ (or $b$) and $c$ directions, respectively.

lower values than in the in-plane direction, which is consistent with the fact that the thermal conduction finds more scattering along this direction due to the weak interaction between layers. In general, the systematic change of atomic masses along this direction increases the phonon scattering (see Fig. 5), which translates in an abrupt reduction of the thermal conductivity.

### D. Elastic constants

Finally, we have calculated the elastic constants using the VASP code, which are obtained from response theory by perturbing the crystallographic vectors from their zero-stress value. The calculated values for $InGaSe_2$ are $C_{11} = 82.3$ GPa, $C_{12} = 34.2$ GPa, $C_{13} = 28.6$ GPa, $C_{22} = 82.3$ GPa, $C_{33} = 76.0$ GPa, $C_{44} = 17.2$ GPa, and $C_{66} = 24.1$ GPa. In the hexagonal system, $c_{66} \equiv (c_{11} - c_{12})/2$, there are only five independent elastic constants. Since all elastic constants are positive, we can confirm that the compound is thermodynamically stable. We can also see that all Born criteria of elastic stability are represented in these data.

By using the obtained elastic constants it is possible to estimate the upper Voigt and lower Reuss bounds for a polycrystalline material for several elastic observables. Here we only give the average value (Hill average) obtained from the two bounds: bulk modulus 47 GPa, shear modulus 21 GPa, and Young modulus of 56 GPa. Our result of the bulk modulus is close to what has been theoretically reported for $\varepsilon$-InSe (44.39 GPa), $\beta$-InSe (44.16 GPa), and $\varepsilon$-GaSe (49.62 GPa) [65,94].

## VII. CONCLUSIONS

In summary, we have performed an *ab initio* calculation of a novel van der Waals heterostructure, namely indium gallium selenide. Though each individual monolayer in the heterostructure happens to be strained, the whole structure becomes energetically, thermally, and elastically stable, a usual behavior in heterostructures formed by layer materials. For this system, we reported the electronic structure and lattice dynamics. We show that this novel structure could have interesting applications, since by engineering InSe/GaSe, we are able of modulate the gap from 1.2 to 2.3 eV (experimental gaps of InSe and GaSe), with open possible applications in solar cells, photodetectors, etc. In the phonon spectra, no imaginary phonons were observed, which indicates the thermal stability of this heterostructure, which probably can be grown by van der Waals epitaxy for instance. Finally, we have calculated the phonon thermal conductivity, which is the most important contribution to the heat transport in the case of semiconductors. From the lower result obtained at room and higher temperatures, we can confirm that $InGaSe_2$ is a promising thermoelectric material due to its low thermal conductivity (for example, it has a value of 1.07 W mK$^{-1}$ at 300 K and 0.55 W mK$^{-1}$ at 600 K), which is comparable with what has been measured in $Bi_2Te_3$, which is one of the best room-temperature thermoelectric materials [95]. The value that we obtain at 600 K compares with the value obtained for SnSe, which has been proven to have outstanding thermoelectric performance at high temperatures [82]. This feature (high ZT at high $T$) makes SnSe, and possibly $InGaSe_2$, suitable for thermoelectric energy conversion, since the operational temperatures are much higher than room $T$. We expect that our work encourages both, experiment and theoretical researchers to further investigate $InGaSe_2$ as a possible high-temperature thermoelectric material.

## ACKNOWLEDGMENTS

We would like to acknowledge the Ministry of Finances and Competitiveness for financial support through Grants No. CSD2010-0044 of the Programme Consolider Ingenio and No. MAT2015-63955-R. We acknowledge the support from the Extreme Science and Engineering Discovery Environment (XSEDE), an organization that is supported by the National Science Foundation Grant No. ACI-1053575, the supercomputer Stampede at the University of Texas and the Bridges supercomputer at the Pittsburgh supercomputer center. A.H.R. acknowledge the support of NSF under Grant No. 1434897. Finally, we thanks the University of Valencia for the use of the supercomputer TIRANT, which belongs to the Red Española de Supercomputación.

[1] V. Sorkin, H. Pan, H. Shi, S. Y. Quek, and Y. W. Zhang, Crit. Rev. Solid State Mater. Sci. **39**, 319 (2014).
[2] Y. Ando, J. Phys. Soc. Jpn. **82**, 102001 (2013).
[3] J. Zhang, C.-Z. Chang, Z. Zhang, J. Wen, X. Feng, K. Li, M. Liu, K. He, L. Wang, X. Chen *et al.*, Nat. Commun. **2**, 574 (2011).
[4] Y. Shi, W. Zhou, A.-Y. Lu, W. Fang, Y.-H. Lee, A. L. Hsu, S. M. Kim, K. K. Kim, H. Y. Yang, L.-J. Li, J.-C. Idrobo, and J. Kong, Nano Lett. **12**, 2784 (2012).
[5] J. N. Coleman, M. Lotya, A. O'Neill, S. D. Bergin, P. J. King, U. Khan, K. Young, A. Gaucher, S. De, R. J. Smith, I. V. Shvets,

S. K. Arora, G. Stanton, H.-Y. Kim, K. Lee, G. T. Kim, G. S. Duesberg, T. Hallam, J. J. Boland, J. J. Wang, J. F. Donegan, J. C. Grunlan, G. Moriarty, A. Shmeliov, R. J. Nicholls, J. M. Perkins, E. M. Grieveson, K. Theuwissen, D. W. McComb, P. D. Nellist, and V. Nicolosi, Science **331**, 568 (2011).
[6] S. Xiong and G. Cao, Nanotechnology **27**, 105701 (2016).
[7] C. Ruppert, O. B. Aslan, and T. F. Heinz, Nano Lett. **14**, 6231 (2014).
[8] J. Huang, W. Wang, Q. Fu, L. Yang, K. Zhang, J. Zhang, and B. Xiang, Nanotechnology **27**, 13LT01 (2016).
[9] C. Gonzlez, B. Biel, and Y. J. Dappe, Nanotechnology **27**, 105702 (2016).
[10] J. Lee, K. Mak, and J. Shan, Nat. Nanotechnol. **11**, 421 (2016).
[11] C. Espejo, T. Rangel, A. H. Romero, X. Gonze, and G.-M. Rignanese, Phys. Rev. B **87**, 245114 (2013).
[12] S. M. Valero, V. García-López, A. Cantarero, and M. Galbiati, Appl. Sci. **6**, 264 (2016).
[13] D.-X. Qu, Y. S. Hor, and R. J. Cava, Phys. Rev. Lett. **109**, 246602 (2012).
[14] C. Rodríguez-Fernández, C. V. Manzano, A. H. Romero, J. Martín, M. Martín-González, M. M. de Lima Jr., and A. Cantarero, Nanotechnology **27**, 075706 (2016).
[15] W. Ibarra-Hernández, M. J. Verstraete, and J.-Y. Raty, Phys. Rev. B **90**, 245204 (2014).
[16] J. Kosmaca, J. Andzane, M. Baitimirova, F. Lombardi, and D. Erts, ACS Appl. Mater. Interf. **8**, 12257 (2016).
[17] E. O. Wrasse and T. M. Schmidt, Nano Lett. **14**, 5717 (2014).
[18] L. Zhang and D. J. Singh, Phys. Rev. B **80**, 075117 (2009).
[19] P. J. Ko, A. Abderrahmane, T. Takamura, N.-H. Kim, and A. Sandhu, Nanotechnology **27**, 325202 (2016).
[20] X. Li, M.-W. Lin, A. A. Puretzky, J. C. Idrobo, C. Ma, M. Chi, M. Yoon, C. M. Rouleau, I. I. Kravchenko, D. B. Geohegan, and K. Xiao, Sci. Rep. **4**, 5497 (2014).
[21] X. Li, L. Basile, M. Yoon, C. Ma, A. A. Puretzky, J. Lee, J. C. Idrobo, M. Chi, C. M. Rouleau, D. B. Geohegan, and K. Xiao, Angew. Chem., Int. Ed. **54**, 2712 (2015).
[22] P. Dey, J. Paul, G. Moody, C. E. Stevens, N. Glikin, Z. D. Kovalyuk, Z. R. Kudrynskyi, A. H. Romero, A. Cantarero, D. J. Hilton, and D. Karaiskaj, J. Chem. Phys. **142**, 212422 (2015).
[23] J. F. Sanchez-Royo, G. Munoz-Matutano, M. Brotons-Gisbert, J. P. Martinez-Pastor, A. Segura, A. Cantarero, R. Mata, J. Canet-Ferrer, G. Tobias, E. Canadell, J. Marques-Hueso, and B. D. Gerardot, Nano Res. **7**, 1556 (2014).
[24] G. W. Mudd, S. A. Svatek, L. Hague, O. Makarovsky, Z. R. Kudrynskyi, C. J. Mellor, P. H. Beton, L. Eaves, K. S. Novoselov, Z. D. Kovalyuk, E. E. Vdovin, A. J. Marsden, N. R. Wilson, and A. Patanè, Adv. Mater. **27**, 3760 (2015).
[25] W. Feng, W. Zheng, X. Chen, G. Liu, and P. Hu, ACS Appl. Mater. Interf. **7**, 26691 (2015).
[26] Z. Ali, M. Mirza, C. Cao, F. K. Butt, M. Tanveer, M. Tahir, I. Aslam, F. Idrees, and M. Safdar, ACS Appl. Mater. Interf. **6**, 9550 (2014).
[27] P. Hu, L. Wang, M. Yoon, J. Zhang, W. Feng, X. Wang, Z. Wen, J. C. Idrobo, Y. Miyamoto, D. B. Geohegan, and K. Xiao, Nano Lett. **13**, 1649 (2013).
[28] S. Zhang, N. Wang, S. Liu, S. Huang, W. Zhou, B. Cai, M. Xie, Q. Yang, X. Chen, and H. Zeng, Nanotechnology **27**, 274001 (2016).
[29] B. Hunt, J. D. Sanchez-Yamagishi, A. F. Young, M. Yankowitz, B. J. LeRoy, K. Watanabe, T. Taniguchi, P. Moon, M. Koshino, P. Jarillo-Herrero, and R. C. Ashoori, Science **340**, 1427 (2013).
[30] S. Dai, Z. Fei, Q. Ma, A. S. Rodin, M. Wagner, A. S. McLeod, M. K. Liu, W. Gannett, W. Regan, K. Watanabe, T. Taniguchi, M. Thiemens, G. Dominguez, A. H. C. Neto, A. Zettl, F. Keilmann, P. Jarillo-Herrero, M. M. Fogler, and D. N. Basov, Science **343**, 1125 (2014).
[31] D. R. Hofstadter, Phys. Rev. B **14**, 2239 (1976).
[32] Y. L. Chen, J. G. Analytis, J.-H. Chu, Z. K. Liu, S.-K. Mo, X. L. Qi, H. J. Zhang, D. H. Lu, X. Dai, Z. Fang, S. C. Zhang, I. R. Fisher, Z. Hussain, and Z.-X. Shen, Science **325**, 178 (2009).
[33] X. Yan, B. Poudel, Y. Ma, W. S. Liu, G. Joshi, H. Wang, Y. Lan, D. Wang, G. Chen, and Z. F. Ren, Nano Lett. **10**, 3373 (2010).
[34] S. Bäßler, T. Böhnert, J. Gooth, C. Schumacher, E. Pippel, and K. Nielsch, Nanotechnology **24**, 495402 (2013).
[35] D. Guo and C. Hu, Appl. Surf. Sci. **321**, 525 (2014).
[36] A. Koma, Thin Solid Films **216**, 72 (1992).
[37] H. D. Li, Z. Y. Wang, X. Kan, X. Guo, H. T. He, Z. Wang, J. N. Wang, T. L. Wong, N. Wang, and M. H. Xie, New J. Phys. **12**, 103038 (2010).
[38] C. Tatsuyama, T. Tanbo, and N. Nakayama, Appl. Surf. Sci. **41-42**, 539 (1990).
[39] R. Schwarcz and M. A. Kanehisa, Solid State Commun. **92**, 689 (1994).
[40] D. Fargues, L. Brahim-Otsmane, M. Eddrief, C. Sbenne, and M. Balkanski, Appl. Surf. Sci. **65-66**, 661 (1993).
[41] F. M. Gashimzade and N. B. Mustafaev, Z. Phys. B: Condens. Matter **99**, 219 (1995).
[42] F. Tran and P. Blaha, Phys. Rev. Lett. **102**, 226401 (2009).
[43] P. E. Blöchl, Phys. Rev. B **50**, 17953 (1994).
[44] G. Kresse and D. Joubert, Phys. Rev. B **59**, 1758 (1999).
[45] G. Kresse and J. Hafner, Phys. Rev. B **47**, 558 (1993).
[46] G. Kresse and J. Hafner, Phys. Rev. B **49**, 14251 (1994).
[47] G. Kresse and J. Furthmüller, Comput. Mater. Sci. **6**, 15 (1996).
[48] G. Kresse and J. Furthmüller, Phys. Rev. B **54**, 11169 (1996).
[49] J. P. Perdew and A. Zunger, Phys. Rev. B **23**, 5048 (1981).
[50] J. P. Perdew, K. Burke, and M. Ernzerhof, Phys. Rev. Lett. **77**, 3865 (1996).
[51] M. Dion, H. Rydberg, E. Schröder, D. C. Langreth, and B. I. Lundqvist, Phys. Rev. Lett. **92**, 246401 (2004).
[52] J. Klimeš, D. R. Bowler, and A. Michaelides, J. Phys.: Condens. Matter **22**, 022201 (2010).
[53] J. Klimeš, D. R. Bowler, and A. Michaelides, Phys. Rev. B **83**, 195131 (2011).
[54] H. J. Monkhorst and J. D. Pack, Phys. Rev. B **13**, 5188 (1976).
[55] A. Togo, F. Oba, and I. Tanaka, Phys. Rev. B **78**, 134106 (2008).
[56] A. Togo, L. Chaput, and I. Tanaka, Phys. Rev. B **91**, 094306 (2015).
[57] P. Blaha, K. Schwarz, G. Madsen, D. Kvasnicka, and J. Luitz, WIEN2K: An augmented plane wave plus local orbitals program for calculating crystal properties users guide, WIEN2K 14.2, (2014).
[58] J. Desclaux, Comput. Phys. Commun. **1**, 216 (1970).
[59] J. Desclaux, Comput. Phys. Commun. **9**, 31 (1975).
[60] D. Errandonea, A. Segura, F. J. Manjón, A. Chevy, E. Machado, G. Tobias, P. Ordejón, and E. Canadell, Phys. Rev. B **71**, 125206 (2005).
[61] A. Mavrokefalos, Q. Lin, M. Beekman, J. H. Seol, Y. J. Lee, H. Kong, M. T. Pettes, D. C. Johnson, and L. Shi, Appl. Phys. Lett. **96**, 181908 (2010).

[62] C. Auriel, R. Roesky, A. Meerschaut, and J. Rouxel, Mater. Res. Bull. **28**, 247 (1993).
[63] S. Haigh, A. Gholinia, R. Jalil, S. Romani, L. Britnell, D. Elias, K. Novoselov, L. Ponomarenko, A. Geim, and R. Gorbachev, Nat. Mater. **11**, 764 (2012).
[64] J. Srour, M. Badawi, F. E. H. Hassan, and A. V. Postnikov, Phys. Status Solidi (b) **253**, 1472 (2016).
[65] L. Ghalouci, B. Benbahi, S. Hiadsi, B. Abidri, G. Vergoten, and F. Ghalouci, Comput. Mater. Sci. **67**, 73 (2013).
[66] V. M. Kaminskii, Z. D. Kovalyuk, M. N. Pyrlya, S. V. Gavrilyuk, and V. V. Netyaga, Inorg. Mater. **41**, 793 (2005).
[67] W. An, F. Wu, H. Jiang, G.-S. Tian, and X.-Z. Li, J. Chem. Phys. **141**, 084701 (2014).
[68] VASP, vdw-df functional of Langreth and Lundqvist *et al.* (2017).
[69] See Supplemental Material at http://link.aps.org/supplemental/10.1103/PhysRevB.96.035201 for the electronic band structure of GaSe and InSe, the electronic DOS calculated with a HSE06 hybrid functional, and the electronic charge density of $InGaSe_2$, as well as the Ga, In, and Se contributions to the DOS in $InGaSe_2$. Finally, we also show the atomic displacements for the other modes present at the Γ point.
[70] D. Olguín, A. Cantarero, C. Ulrich, and K. Syassen, Phys. Status Solidi (b) **235**, 456 (2003).
[71] S. Nagel, A. Baldereschi, and K. Maschke, J. Phys. C **12**, 1625 (1979).
[72] D. V. Rybkovskiy, N. R. Arutyunyan, A. S. Orekhov, I. A. Gromchenko, I. V. Vorobiev, A. V. Osadchy, E. Y. Salaev, T. K. Baykara, K. R. Allakhverdiev, and E. D. Obraztsova, Phys. Rev. B **84**, 085314 (2011).
[73] L. C. Dacal and A. Cantarero, Solid State Commun. **151**, 781 (2011).
[74] S. Y. Sarkisov, A. V. Kosobutsky, V. N. Brudnyi, and Y. N. Zhuravlev, Phys. Solid State **57**, 1735 (2015).
[75] S. G. Choi, D. H. Levi, C. Martinez-Tomas, and V. M. Sanjos, J. Appl. Phys. **106**, 053517 (2009).
[76] Bilbao crystallographic server.
[77] A. Cantarero, J. Nanophoton. **7**, 071598 (2013).
[78] N. M. Gasanly, A. Aydınlı, H. Özkan, and C. Kocabaş, Mater. Res. Bull. **37**, 169 (2002).
[79] P. Dey, J. Paul, N. Glikin, Z. D. Kovalyuk, Z. R. Kudrynskyi, A. H. Romero, and D. Karaiskaj, Phys. Rev. B **89**, 125128 (2014).
[80] J. Carrete, N. Mingo, and S. Curtarolo, Appl. Phys. Lett. **105**, 101907 (2014).
[81] A. Dewandre, O. Hellman, S. Bhattacharya, A. H. Romero, G. K. H. Madsen, and M. J. Verstraete, Phys. Rev. Lett. **117**, 276601 (2016).
[82] L.-D. Zhao, G. Tan, S. Hao, J. He, Y. Pei, H. Chi, H. Wang, S. Gong, H. Xu, V. P. Dravid, C. Uher, G. J. Snyder, C. Wolverton, and M. G. Kanatzidis, Science **351**, 141 (2016).
[83] O. Pavlic, W. Ibarra-Hernandez, I. Valencia-Jaime, S. Singh, G. Avendaño-Franco, D. Raabe, and A. H. Romero, J. Alloys Compd. **691**, 15 (2017).
[84] P. Anees, M. C. Valsakumar, S. Chandra, and B. K. Panigrahi, Modell. Simul. Mater. Sci. Eng. **22**, 035016 (2014).
[85] H. Zabel, W. A. Kamitakahara, and R. M. Nicklow, Phys. Rev. B **26**, 5919 (1982).
[86] S. Singh, W. Ibarra-Hernandez, I. Valencia-Jaime, G. Avendano-Franco, and A. H. Romero, Phys. Chem. Chem. Phys. **18**, 29771 (2016).
[87] H. Zabel, J. Phys.: Condens. Matter **13**, 7679 (2001).
[88] K. H. Michel and B. Verberck, Phys. Status Solidi (b) **249**, 2604 (2012).
[89] C. Adler, R. Honke, P. Pavone, and U. Schröder, Phys. Rev. B **57**, 3726 (1998).
[90] S. Jandl, J. L. Brebner, and B. M. Powell, Phys. Rev. B **13**, 686 (1976).
[91] J. Garg, N. Bonini, and N. Marzari, in *Length-Scale Dependent Phonon Interactions*, edited by G. P. S. S. L. Shindé, Topics in Applied Physics Vol. 128 (Springer, New York, 2014), pp. 115–136.
[92] N. Mingo, D. A. Stewart, D. A. Broido, L. Lindsay, and W. Li, in *Length-Scale Dependent Phonon Interactions*, edited by G. P. S. S. L. Shindé, Topics in Applied Physics Vol. 128 (Springer, New York, 2014), pp. 137–173.
[93] M. Culebras, C. M. Gómez, and A. Cantarero, Materials **7**, 6701 (2014).
[94] L. Ghalouci, F. Taibi, F. Ghalouci, and M. Bensaid, Comput. Mater. Sci. **124**, 62 (2016).
[95] C. B. Satterthwaite and R. W. Ure, Phys. Rev. **108**, 1164 (1957).